

pubs.acs.org/JPCC Article

# Atomic Level Insight into the Nucleation of SnSe Thin Films Using Graphene Mask in Molecular Beam Epitaxy: ReaxFF Molecular Dynamics Simulations

Benazir Fazlioglu-Yalcin, Mengyi Wang, Nadire Nayir, Stephanie Law, and Adri C. T. van Duin\*



Cite This: J. Phys. Chem. C 2024, 128, 14294-14304



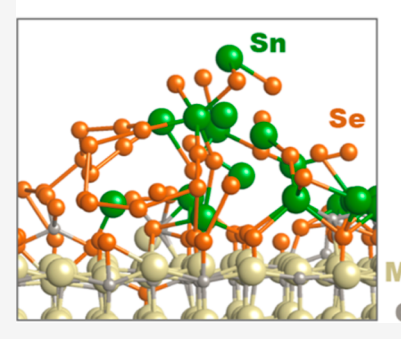
**ACCESS** 

Metrics & More

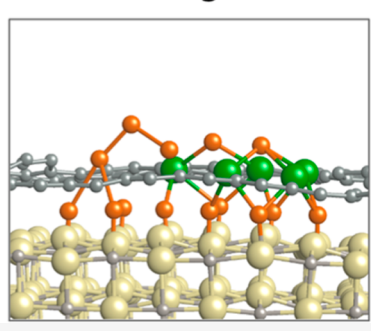
Article Recommendations

Supporting Information

# Bare substrate



# Masked growth



**ABSTRACT:** The controlled growth of thin films plays a crucial role in tailoring material properties for diverse applications. Overcoming challenges in thin film fabrication, such as island growth modes and morphological irregularities, is essential for optimizing overall material and device performance. Here, we report the atomic-level investigation of the controlled nucleation of SnSe on a MgO(001) substrate through molecular beam epitaxy, using ReaxFF reactive molecular dynamics simulations. Using graphene masks for selective area nucleation, we explore the effects of mask usage and mask thickness on the morphology of the deposited SnSe material. A key finding is that a single-layer graphene mask promotes the formation of the crystalline  $P\overline{3}m1$  phase of SnSe<sub>2</sub> during nucleation. Additionally, by using multiple thermostats in our simulations we can mitigate gas-phase Sn<sub>x</sub>Se<sub>y</sub> clustering and ensure a more accurate representation of molecular beam epitaxy conditions. The incorporation of multiple thermostats in the simulations contributes to a deeper understanding of the nucleation mechanism. Overall, this study provides atomic-level insight into the selective area nucleation technique for thin film deposition processes.

# 1. INTRODUCTION

Tin-based binary chalcogenides, particularly SnSe, have attracted considerable scientific interest due to their wide range of applications, from electronic devices to energy harvesting systems. 1-4 The Pnma phase of SnSe has a layered orthorhombic structure characterized by a large in-plane anisotropy. 5 This anisotropy leads to an exceptional ratio of carrier mobility ( $\sim$ 5.8), setting a new record for high anisotropic mobility among 2D materials.<sup>6,7</sup> The anharmonicity of vibrational modes in the SnSe lattice contributes to the ultralow thermal lattice conductivity, giving SnSe a high figure of merit and making it a promising thermoelectric material.<sup>8,9</sup> Known for its suitable band gap ( $\sim 0.9-1.5$  eV), high optical absorption coefficient ( $\sim 10^5$  cm<sup>-1</sup>), earth abundance, and low toxicity, SnSe is also being explored as a candidate absorber material for next-generation solar cells. 10-12

SnSe thin films exhibit high sensitivity to deposition and growth conditions, impacting crucial material properties such

as band gap, carrier concentration, and carrier mobility. <sup>13</sup> To date, various deposition techniques including atomic layer deposition (ALD), <sup>14,15</sup> thermal evaporation, <sup>16</sup> hot wall epitaxy, <sup>17</sup> chemical vapor deposition (CVD), <sup>18,19</sup> and spray pyrolysis <sup>20,21</sup> have been employed for the synthesis of SnSe. Growth parameters such as substrate type, growth temperature, precursor concentration ratio, and deposition rate play a critical role in controlling the film composition, uniformity, thickness, surface morphology, and crystallinity, which are the common factors determining the quality of SnSe. <sup>22–24</sup> Furthermore, achieving optimal device performance is intricately linked to the precise control of all these parameters,

Received: May 10, 2024 Revised: August 1, 2024 Accepted: August 2, 2024 Published: August 19, 2024





which requires an atomic-level understanding of the growth mechanism. To gain deeper insight into the synthesis of SnSe, a material extensively used for various applications as mentioned above, it is clear that there is a need for an investigation to unveil its growth mechanism under specific conditions using computational tools.

In a recent study, Chin et al. used molecular beam epitaxy (MBE) to grow SnSe thin films on a MgO(001) substrate with a wide range of precursor flux ratios.<sup>25</sup> They observed that the films feature large lateral grains with a pyramidal growth habit rather than the desired layer-by-layer growth mode, with additional computational insight into the initial stages of growth in the absence of a substrate. The growth of SnSe epitaxial films on MgO substrates exhibited a high density of twin boundaries with square symmetry, leading to degeneracy between SnSe 90° domain orientations.<sup>26</sup> Frezza et al. observed the growth of a monolayer of  $\beta$ -SnSe (space group Cmcm) on an Au(111) substrate, followed by the subsequent formation of islands of  $\alpha$ -SnSe (space group *Pnma*) on top of the monolayer.<sup>27</sup> Zhang et al. demonstrated the adaptability of SnSe<sub>2</sub> thin films to either a quasi-layered or island growth mode, depending on the chemical nature of the substrate.<sup>28</sup> These observations underscore the significant challenges in epitaxial growth, where surface energy, interfacial interactions, and adatom mobility collectively contribute to undesirable island growth modes and hinder the desired coalescence into uniform and continuous films.

To address nonuniformity in thin films, a mask can be used to facilitate selective area nucleation and growth. This method involves shielding specific regions of the substrate from precursors, thereby confining nucleation sites to predetermined areas. The goal is to mitigate variations in nucleation sites and growth rates in order to prevent nonuniformity in thin films. Such an approach facilitates the controlled growth of a single grain within a specific region around which a device can be patterned, thereby eliminating grain boundary scattering. This technique has been successfully applied to the MBE growth of various III-V semiconductor nanostructures and thin films. 29-41 However, an atomic-level understanding of the controlled nucleation and growth of SnSe is currently missing. To fill this knowledge gap, we selected molecular dynamics as our approach to study the formation of the initial layers of SnSe on a substrate for the first time, within a computationally reasonable time scale. Specifically, we chose the ReaxFF reactive force field, 42 which has been shown to effectively model bond formation and breaking, to observe the precursors during growth as they deposit onto a MgO(001) substrate using a graphene mask. Due to its chemical inertness, the graphene mask was selected to reduce surface interactions with precursors during deposition. This approach effectively confined the nuclei within the holes formed in the graphene, promoting more controlled and localized nucleation. The chemically inert nature of graphene prevented unwanted reactions with the precursors, ensuring that the nucleation process was confined to the predefined areas. Additionally, to accurately simulate the conditions observed in experimental MBE setups, mixed thermostats were employed in the simulations. This strategy helped to mitigate undesired gasphase clustering in a vacuum environment, replicating the thermal conditions that prevent precursor aggregation and ensuring uniform nucleation and growth of SnSe structures.

#### 2. METHODS

**2.1. ReaxFF Force Field.** ReaxFF<sup>42,43</sup> employs a bond order formalism, enabling the simulation of bond breakage and formation over the course of the simulations. Consequently, the ReaxFF force fields have proven to be a practical tool for simulating the nucleation and growth of thin film materials, addressing gas-phase and surface interactions influenced by the surrounding chemical environment, and facilitating the prediction of effective growth protocols.<sup>44</sup>

**2.2. Force Field Development.** We extended the ReaxFF force field framework developed by Chin et al.<sup>25</sup> to Sn/Se/ Mg/O/C interactions to explore the atomic-level nucleation process of SnSe thin films on (001) MgO substrates (space group  $Fm\overline{3}m$ ) with a graphene mask. The training data set from ref 25 includes heats of formation and equations of state for various condensed phases, such as bulk alpha-Sn, orthorhombic (Pnma) SnSe, cubic (Fm3m) SnSe, and trigonal (P3m1) SnSe<sub>2</sub>. It also includes binding energies of various Sn<sub>x</sub>Se<sub>y</sub> clusters with different Sn/Se ratios. We augmented this data set with density functional theory (DFT) data on the binding energies of Sn and Se atoms to three distinct adsorption sites on MgO. Then, in addition to refining the existing parameters, we carried out optimization on parameters related to Sn-O, Se-O, Sn-Mg, Se-Mg associated bonds, off-diagonal elements, angles, and torsions during the training process against the DFT-based data set. In this training, the Mg/O related parameters were adopted from the Na/Ca/Mg/ C/O/H force field developed by Dasgupta et al.45 The parameters pertaining to the C-C and C-O bond, valence angle and dihedral angle interactions were taken from ref 46. For the C-Se, C-Sn and C-Mg pairs, we only considered nonbonded Coulomb and van der Waals interactions-the covalent bond interactions between these atoms were switched off. As such, in this study, the edges of a graphene mask would not chemically interact with Se, Sn, or Mg.

DFT calculations were carried out using the Vienna Ab initio Simulation Package (VASP)<sup>47–49</sup> employing projector augmented wave method pseudopotentials.<sup>50,51</sup> The generalized gradient approximation (GGA) of Perdew-Burke-Ernzerhof (PBE)<sup>52</sup> was utilized to describe the exchange correlation function. Plane-wave expansions were truncated at an energy cutoff of 500 eV, and the electronic loop threshold was set at 0.1 meV. Structural relaxations incorporated dipole corrections to the total energy and electrostatic potential in the out-of-plane direction, ensuring that the remaining forces were within 0.01 eV Å<sup>-1</sup>. Gaussian smearing with a broadening of 0.02 eV was applied, and van der Waals interactions were addressed using the semiempirical correction of Grimme (zero damping DFT-D3).53 Brillouin zone samplings were performed with a Γ-centered Monkhorst-Pack scheme on grids featuring k-point densities equivalent to a  $4 \times 4 \times 1$  grid for a 1 × 1 c-plane MgO unit cell. To minimize spurious interactions of periodic repetitions, a vacuum layer of 20 Å was introduced normal to the surface.

**2.3. ReaxFF Molecular Dynamics Simulations.** We performed ReaxFF molecular dynamics (MD) simulations using the newly developed force field with the AMS software platform. The dimensions of the simulation boxes were 21 Å  $\times$  63 Å  $\times$  90 and 21 Å  $\times$  63 Å  $\times$  120 Å, with periodic boundary conditions applied in all three dimensions. A free-standing graphene mask with 1–4 layers was positioned on MgO with a distance of 3.2 Å between the mask and the substrate. A hole

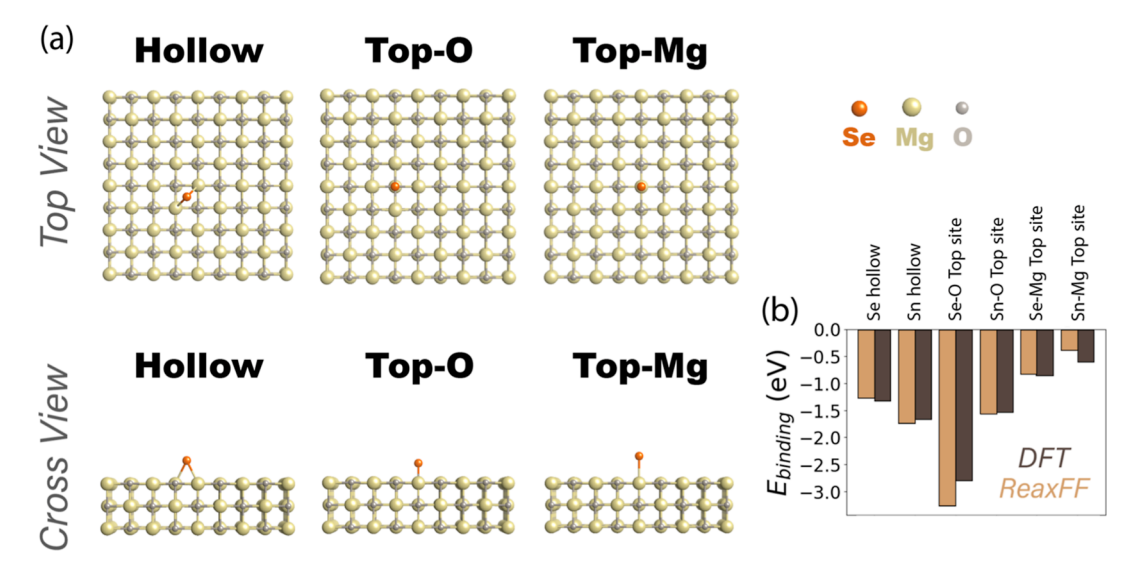


Figure 1. (a) Illustration of Se atoms occupying the hollow position in an MgO lattice, on top of O, and on top of Mg, shown in top and cross views. (b) Comparative ReaxFF and DFT binding energies for Sn and Se atoms at different positions. Similar binding sites were employed for Sn atoms, although only Se atoms are shown in (a) for clarity.

was introduced into the graphene by removing 24 C atoms from its center. The whole system was then exposed to Sn and Se precursors, adopting the Sn/Se ratio of 1:4 commonly used in experiments.<sup>25</sup> (See Supporting Information, Figure S1).

After energy minimization, the system was heated to 500 K in an NVT ensemble. The velocity Verlet algorithm was employed with a time step of 0.25 fs or smaller to integrate the Newton equations of motion. The total simulation time was set to 50, 125, 250, and 1000 ps for different simulations. The Berendsen thermostat was used to control temperature fluctuations, and two different thermostat setups were studied in our simulations: a single thermostat and a mixed thermostat, which aimed to mimic experimental setups of MBE systems.

In simulations with a single thermostat, a temperature damping parameter of 100 fs was applied to ensure strict temperature control throughout the system. In contrast, in mixed thermostat simulations, the bottom 12 layers of the substrate (bulk MgO) were heated with a temperature damping parameter of 100 fs, while the precursors, the graphene layer, and the first 4 layers of the substrate surface were subjected to a very weak thermostat with a temperature damping parameter of 10<sup>7</sup> fs. This methodology was chosen based on the placement of substrates inside an MBE chamber, where the back side of the substrate is in direct contact with the heater, effectively reaching the target temperature. On the other hand, the upper part of the substrate, the mask, and the precursors are away from the heater, resulting in diminished thermal control in these areas.

# 3. RESULTS & DISCUSSION

**3.1. Force Field Development for Sn/Se Interactions with MgO.** Figure 1a,b depict the geometries and ReaxFF predicted binding energies of three distinct adsorption sites: the top of magnesium (Top-Mg), the top of oxygen (Top-O), and the hollow site. According to the ReaxFF results, the top-O site and hollow site are the most thermodynamically favorable sites for the binding of Se and Sn atoms to the surface, respectively. Furthermore, the top-Mg site is a thermodynamically less stable adsorption site for both Se

and Sn atoms. These results are in good agreement with those obtained at the DFT level in Figure 1b.

**3.2.** Nucleation of SnSe on MgO with and without a Graphene Mask. Recent experimental studies have highlighted challenges in SnSe thin film growth. These challenges include issues such as nonuniformity in the SnSe crystal phase, complex stoichiometry control, 3D island nucleation, and the resulting formation of noncoalesced thin films. Here, adatom mobility is a crucial factor in facilitating the free movement of precursor atoms across the substrate surface to form a coalesced thin film. However, when adatom mobility is insufficient, films do not grow in a coalesced manner, leading to island-like growth on the surface.

In line with the experimental observations, the ReaxFF simulations showed that the nucleation of SnSe on a bare MgO substrate resulted in surface nonuniformity where a random distribution of nucleation sites was observed, and the size of the domains nucleated on the surface remained uncontrollable (Figure 2a). The Sn<sub>x</sub>Se<sub>y</sub> clusters formed on the surface did not have a discernible crystal structure. Additionally, the highlighted section in the middle of Figure 2a revealed the out-of-plane diffusion of an oxygen atom from the substrate, which participated in bonding interactions with Sn and Se. This behavior has been reported in experiments where diffusion at the film—substrate interface has been observed.<sup>25</sup> Overall, our observation is consistent with experimental findings, highlighting the challenges associated with achieving high-quality SnSe structures.

The system in Figure 2a was further exposed to additional gas phase precursors consisting of 40 Sn and 160 Se atoms, resulting in the MgO surface being covered by SnSe structure. Similar to Figure 2a, the formed structure lacked distinct crystalline phases (Supporting Information, Figure S2). In addition, the precursors tended to cluster in an irregular manner on the MgO surface. This irregular deposition of SnSe is of concern as it deviates from the controlled nucleation process that is essential for achieving high quality thin films. These findings underscore the critical need to address and rectify such irregularities during the nucleation phase to improve the quality of the resulting thin films.

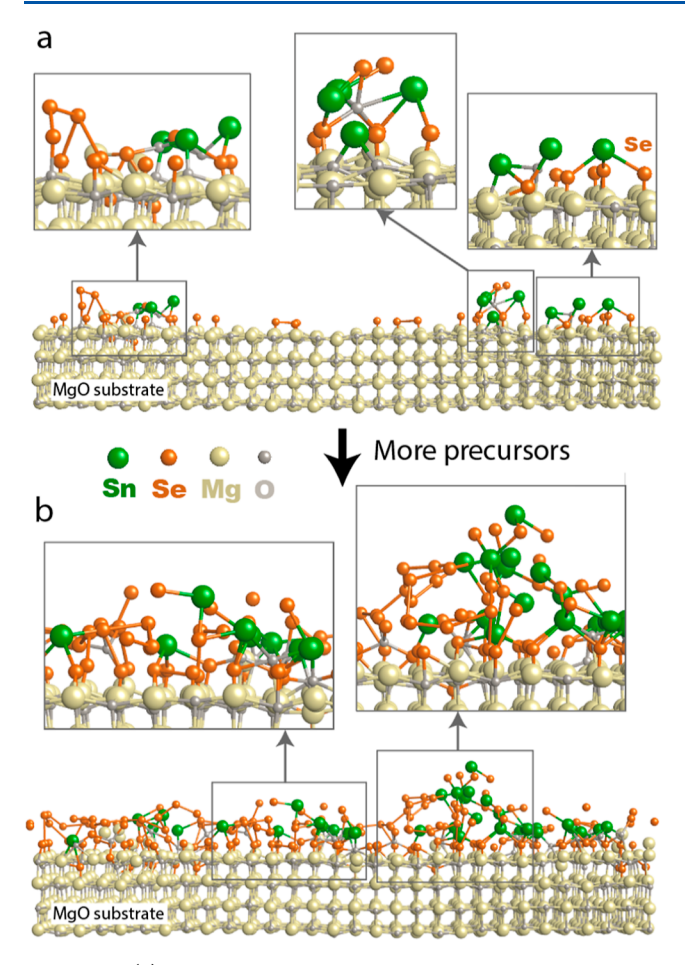


Figure 2. (a) Snapshots taken from the final frame of an MD simulation with 10 Sn and 40 Se atoms deposited on MgO, after 125 ps at 500 K. SnSe nucleation on a bare MgO substrate revealed island-like formations with no discernible crystalline preference. (b) Exposure of the surface to additional precursors complicated the SnSe formation and resulted in an amorphous phase. This figure illustrates the atoms chemically bonded to the substrate, while unreacted atoms and clusters in the vacuum are intentionally excluded from the depiction. This convention is consistently followed in all subsequent simulations presented in this study.

To enhance our understanding of the early stages of nucleation and to investigate the impact of confining nucleation to a specific region, we used a graphene mask with a hole placed on the top of MgO. This hole was created by removing 24 carbon atoms to form a circular shape (about 1.5 nm in diameter) as depicted in Figure 3. The entire system was then exposed to gas phase precursors consisting of 10 Sn and 40 Se atoms.

During nucleation, the confined area of MgO within the hole served as nucleation sites for precursors. This facilitated the migration of monatomic and diatomic gas-phase species toward the graphene hole, subsequently leading to the chemisorption of Sn<sub>x</sub>Se<sub>y</sub> species onto the MgO surface through the vacancy (Figure 3). Another noteworthy result is that in the early stage of the simulation, Se-rich conditions always drove the surface passivation by Se atoms, followed by the Sn interactions with the first Se layer (Figure 3). Under local metal-rich conditions, Sn atoms attached to the surface first. However, the subsequent deposition of Se atoms displaced the Sn atoms from the MgO surface, as shown in Figure 3g. The DFT and ReaxFF calculations in Figure 1 provide additional

support for this observation, showing that Se exhibited stronger binding strength to the substrate in comparison to Sn, supporting the favorable selection of Se as the initial layer. Eventually, the confinement of the MgO surface within the hole drove the transition from an amorphous Sn<sub>x</sub>Se<sub>y</sub> cluster formed in vacuum to the layer-by-layer nucleation of the SnSe<sub>2</sub> structure shown in Figure 3h. The crystal structure of the grown domain within the hole was characterized by a  $P\overline{3}m1$ like phase, in agreement with experimental observations where XRD results highlighted the prevalence of the  $P\overline{3}m1$  crystal phase during the nucleation stage.<sup>25</sup> This pattern was reproduced in ten additional simulations (See Supporting Information, Figure S3), with the SnSe<sub>2</sub> structure featuring a Sn layer sandwiched between two Se layers when the local precursor density was sufficiently high to form a multilayer structure. It is also noteworthy that, due to the high local concentration of selenium, the resultant SnSe2 structure in Figure 3h showed the binding of excess selenium atoms to the grown SnSe<sub>2</sub> structure. Furthermore, in the nucleation process, Se showed a thermodynamic preference for attaching on the top of the O atom of MgO, as confirmed by the DFT calculations illustrated in Figure 1. This analysis of masked SnSe<sub>2</sub> nucleation contributes to an underlying atomistic-level understanding of the challenges associated with controlled nucleation.

3.3. Increased Density of Precursors. To investigate the influence of the precursor concentration on nucleation, we introduced an increased number of precursors comprising 20 Sn and 80 Se atoms into a  $21 \times 63 \times 120 \text{ Å}^3$ ; simulation box. The inclusion of additional precursors led to the formation of larger amorphous clusters in vacuum, as shown in Figure 4a. These clusters then adhered to nuclei on the MgO surface, as shown in Figure 4b,c. Subsequently, the confined nucleation sites on the MgO surface assisted in guiding the partial structural transformation of the Sn<sub>x</sub>Se<sub>y</sub> amorphous cluster to a more crystalline form on the surface (Figure 4c). This transformation continued over time (Figure 4d,e), resulting in the first layer composed of Se atoms. As evident in Figure 4f, this evolved structure displays a resemblance to the P3m1phase of SnSe<sub>2</sub>, similar to the observation in Figure 3. However, the parts of the Sn<sub>x</sub>Se<sub>y</sub> cluster far from the surface retained their amorphous character due to the absence of interactions from the MgO surface and the mask. This signifies the confinement effect of the graphene mask and the potential catalytic role of surface chemistry in the structural transformation of SnSe into a crystalline form. Similar nucleation mechanisms have been reported in previous studies. 56-

**3.4. Multiple Layers of Graphene Mask.** Previous studies have demonstrated that modifying the thickness of a mask is an effective way to manipulate the structure of semiconductor thin films grown on a substrate, and therefore the fabrication of nanowires using a multilayer mask has attracted increasing attention. In this section, we investigated the relationship between mask thickness and the structure of the resulting  $Sn_xSe_y$  clusters nucleated within the graphene mask. Our approach employs a graphene mask with 2, 3, and 4 layers, as shown in Figure 5a–e, in a simulation box with dimensions of  $21 \times 63 \times 120$  ų. In the case of masks with 2 and 3 layers (Figure 5a,b), SnSe nucleation on MgO followed a layer-by-layer nucleation mechanism, resulting in a  $P\overline{3}m1$ -like phase of  $SnSe_2$ , similar to the monolayer graphene models discussed in previous sections. However, with increasing mask thickness,  $Sn_xSe_y$  underwent vertical growth

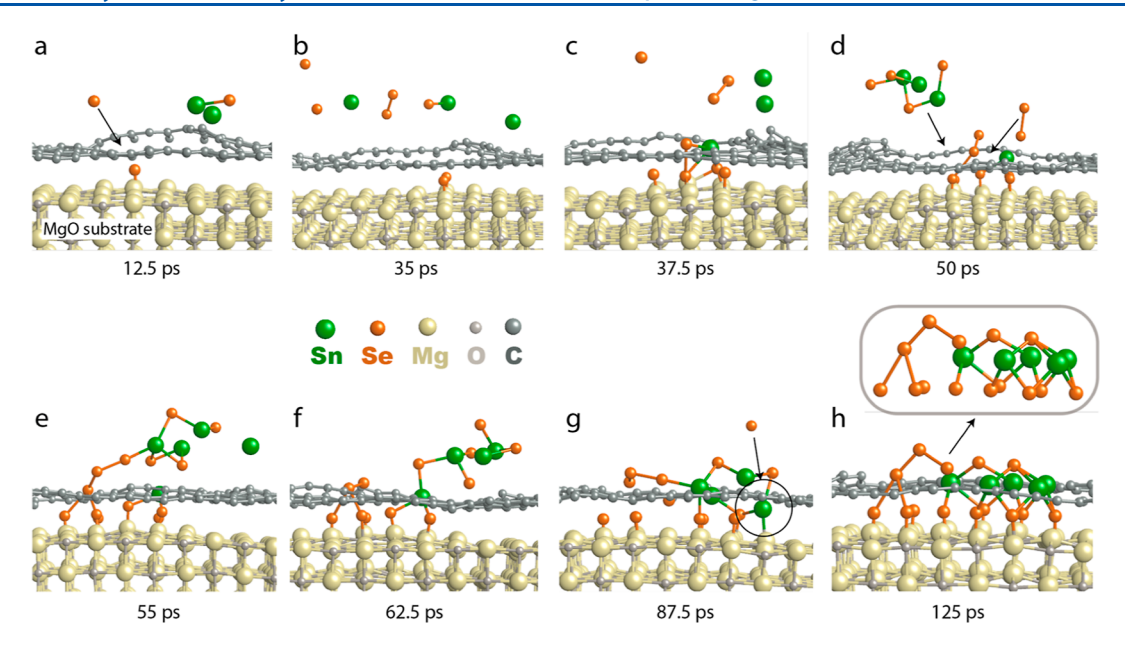


Figure 3. 10 Sn and 40 Se atoms were used as precursors for  $SnSe_2$  nucleation with a graphene mask. The growth temperature was set at 500 K with a total duration of 125 ps. The use of the mask confined the nucleation to a selective area, and the nucleation extended as wide as the hole created in the graphene. The snapshots, labeled from "a" to "h", were arranged in chronological order, with the corresponding simulation time listed below each frame.

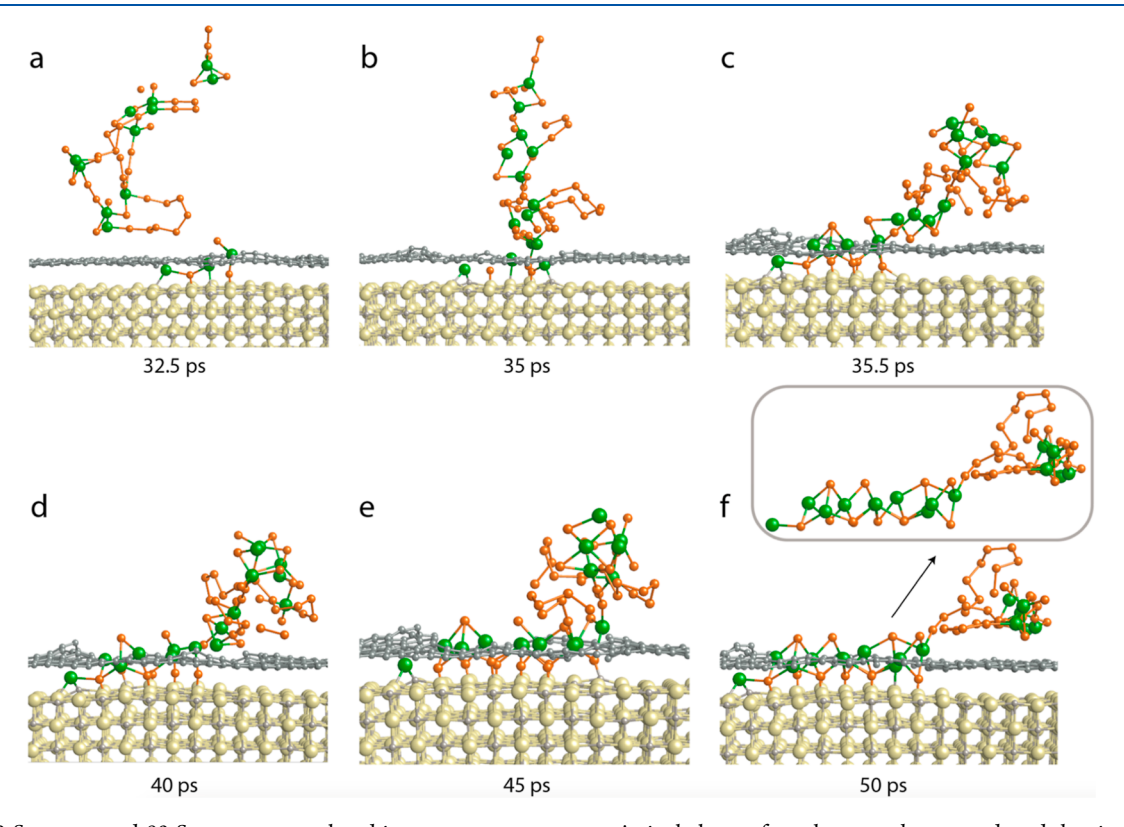


Figure 4. 20 Sn atoms and 80 Se atoms were placed in vacuum as precursors. A single layer of graphene mask was used, and the simulation time was 50 ps. (a-f) A large cluster formed in the vacuum fell through the hole, and the previously amorphous structure gained crystallinity as it formed bonds with the substrate. The parts of the structure that were not in direct contact with the substrate remained amorphous.

within the hole, adopting an amorphous island, as shown in Figure 5c—e. Despite the rod-like growth, the evolving configuration could not be attributed to any particular crystal structure.

Comparative analysis shows that a single layer of graphene stands out as a more favorable mask for the nucleation of 2D

crystalline SnSe<sub>2</sub> structures compared to multilayer graphene masks. The use of multiple layers of graphene poses a distinct challenge in achieving the desired crystalline quality. The use of multiple layers tends to promote the growth of 3D rod-like phases that lack crystalline features. This limitation might have arisen from the hindered direct access of the growing structure

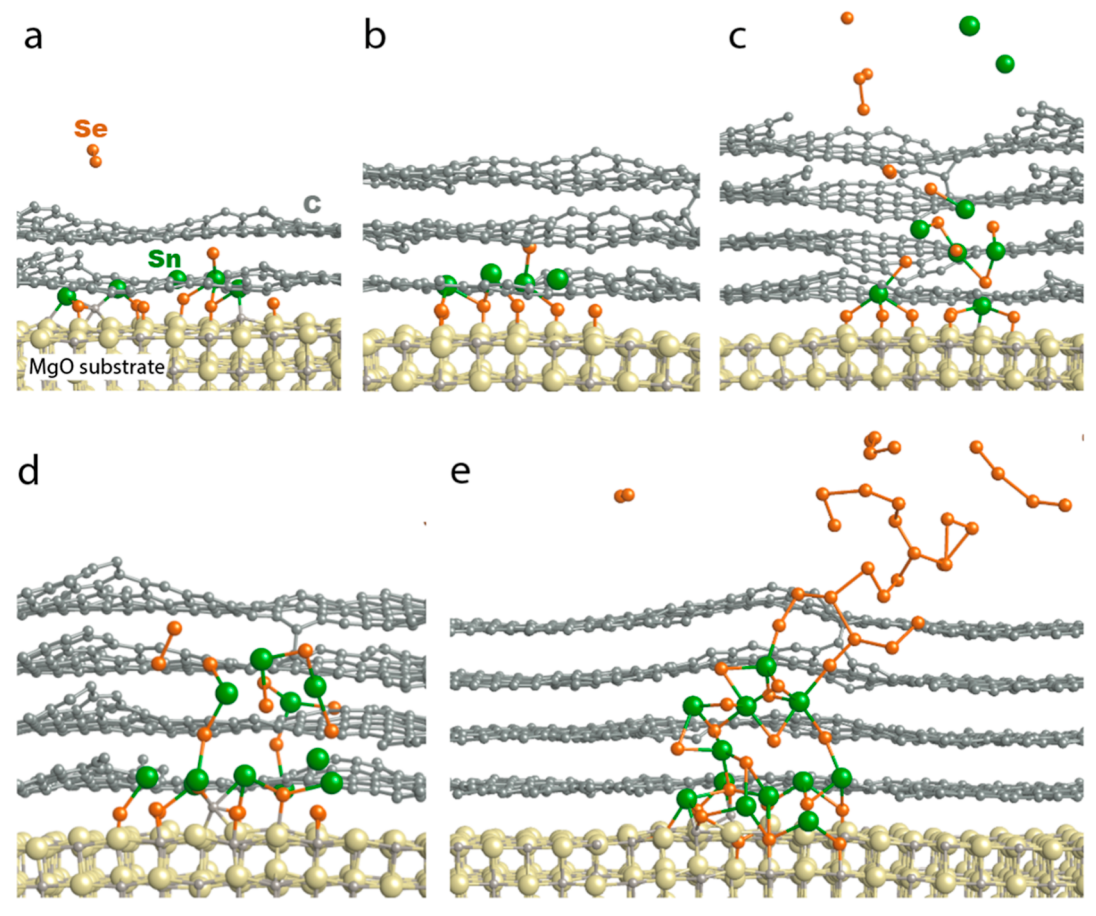


Figure 5. (a) Two and (b) three layers of graphene were used for simulations with 10 Sn and 40 Se atoms as precursors at 500 K. (c,d), and (e) show simulations with four layers of graphene, where (d) continued from (c) with an additional 10 Sn and 40 Se atoms, and (e) continued from (d) with another 10 Sn and 40 Se atoms. In (a,b), layer-by-layer SnSe growth was observed. This pattern continued in the initial stages of (c,d), but after forming three atomic layers of SnSe, amorphization occurred. In (e), rod-like growth was observed, with the amorphous structure extending beyond the masks to the top graphene layer. The frames represent the results of simulations at 330, 266, 50, 228, and 342 ps, respectively.

to the substrate, impeding the precise attachment of precursors at appropriate angles. As a result, the observed transition from 2D to 3D growth with increased mask thickness suggests a fundamental change in the growth mechanism. This transition highlights the importance of mask design in semiconductor fabrication, where achieving a balance between mask thickness and desired film properties is crucial for experimental setups.

3.5. Strong and Weak Thermostat Effect. In scenarios that require the use of highly reactive precursors such as Se, heating of Se sources induces the formation of Se clusters that subsequently reach the substrate surface during growth. This in turn degrades the precision of atom-by-atom growth. 63 Conversely, the sticking coefficients of Se decrease at elevated temperatures, posing a significant challenge to maintaining a stable flow of atomic flux. <sup>64</sup> The cracker stage, implemented in effusion cells, serves as a flux controller in MBE systems by cracking the sources and clusters before they flow onto the substrate. 63 Additionally, the extremely dilute concentration of gas phase molecules in the MBE chamber prevents the formation of large Sn<sub>x</sub>Se<sub>y</sub> clusters. In simulations, thermostats serve as an effective tool to control temperature and thus energy fluctuations within systems. This control, in turn, influences the cluster size, enabling us to mimic MBE conditions in simulations.

In this section, we investigated the effect of thermostat settings on clustering by using strong and weak thermostats in gas phase simulations, as shown in Figure 6a,b. In these simulations, the box dimensions were fixed at  $21 \times 63 \times 120$  Å<sup>3</sup>. Note that all other parameters were kept the same in the two simulations; the only variation was in the temperature damping parameters, which were set to 100 fs for a strong thermostat in Figure 6a and  $10^7$  fs for a weak thermostat in Figure 6b.

Keeping both systems at 500 K for 125 ps, our simulations revealed distinct outcomes depending on the strength of the thermostat applied. In Figure 6a, the use of a strong thermostat led to pronounced clustering in a vacuum, whereas the system subjected to a weak thermostat exhibited a significant reduction in both the size and number of clusters in Figure 6b.

The corresponding plot in Figure 6c provides a more detailed insight into the scenario shown in Figure 6a, emphasizing the formation of diverse molecular species, including 1 Sn<sub>1</sub>, 3 Se<sub>1</sub>, 1 Se<sub>2</sub>, 1 SnSe, 3 Se<sub>3</sub>, 1 SnSe<sub>2</sub>, 1 Sn<sub>2</sub>Se<sub>3</sub>, and 1 SnSe<sub>4</sub>. In contrast, the system subjected to the weak thermostat yielded a distinctly different outcome in Figure 6d, producing mostly atomic species, including 5 Sn<sub>1</sub>, 11 Se<sub>1</sub>, 3 Se<sub>2</sub>, 1 SnSe, and 2 Se<sub>3</sub>, with the notable absence of most Sn<sub>x</sub>Se<sub>y</sub> clusters in Figure 6c. In this context, the thermostat setting significantly influences the size and distribution of the clusters. A weak thermostat setting results in a relatively mild impact on the system temperature, achieved by minimizing energy exchange with an external reservoir.

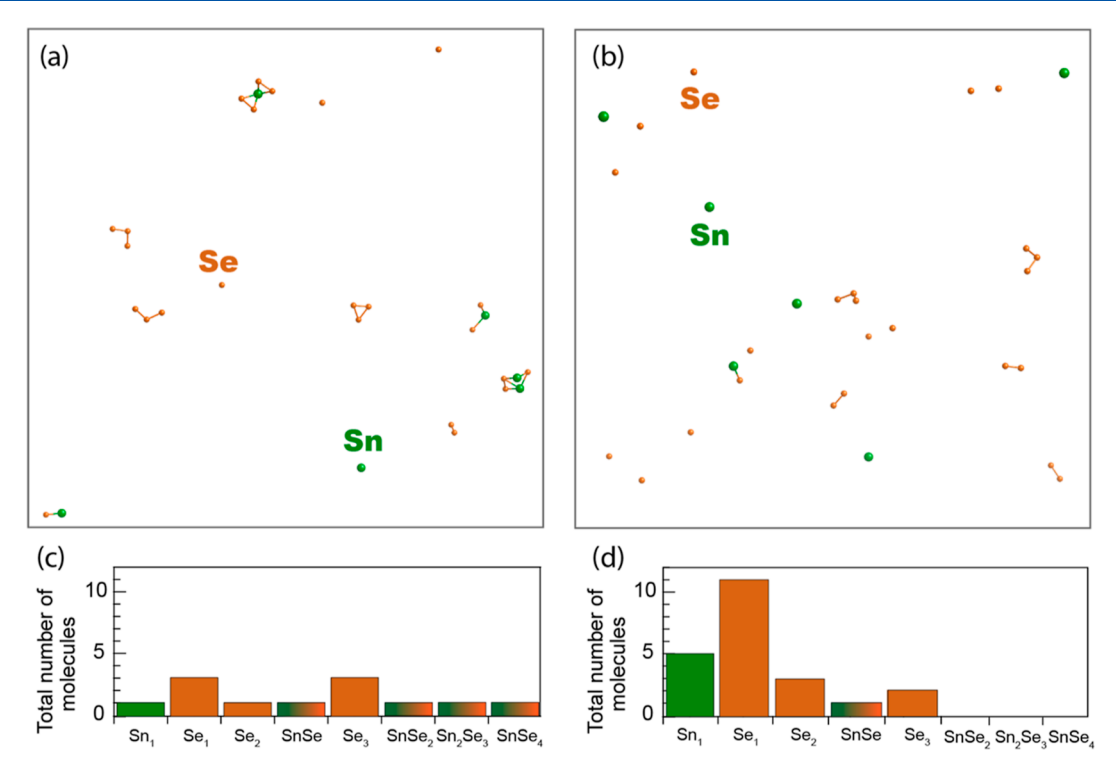


Figure 6. 6 Sn and 24 Se atoms were randomly placed in both simulation boxes shown in (a,b). In (a), a temperature damping parameter of 100 fs was used for the thermostat, while in (b) the temperature damping parameter was set to 10<sup>7</sup> fs. The plots in (c,d) highlight the distribution of clusters formed in the vacuum at the end of 125 ps for each case.

This, in turn, leads to less constrained local temperature fluctuations. In the case of an exothermic reaction such as Sn—Se bond formation, the increase in local temperature reduces the thermodynamic driving force for further reactions—in particular bond dissociation. Consequently, the implementation of a weak thermostat resulted in a significant reduction of clustering throughout the simulation. On the other hand, a stronger thermostat maintains the system temperature more strictly through frequent energy exchange with a heat bath, allowing more reactions to occur in vacuum due to the rapid removal of kinetic energy generated by exothermic reactions. Although the simulations presented here are relatively small, they were performed multiple times to ensure reproducibility. Future work will include larger-scale simulations to further validate our findings.

This observation demonstrates the effectiveness of using a weak thermostat to create optimal conditions similar to the MBE technique. The strategic use of a weak thermostat not only leads to a significant reduction in clustering within the system, but also promotes the prevalence of single atomic species. The interplay between the weak thermostat setting and the resulting MD in the vacuum environment suggests a more controlled and ordered growth scenario during MBE processes. This favorable outcome, characterized by minimized clustering and the predominance of single atomic species, is consistent with the objectives of achieving precise control over material deposition and enhancing the quality of thin film growth. Strategic modulation of the thermostat strength emerges as a key factor in tailoring the growth conditions, highlighting its potential as a valuable parameter in optimizing MBE processes for advanced materials fabrication.

Motivated by the impact of weak and strong thermostats on gas phase dynamics, we extended this approach to explore the SnSe nucleation mechanism on MgO. As illustrated in Figure

7a, the simulation was divided into four different zones, each subjected to distinctive thermostat settings. The yellow zone represents the precursors, the green zone corresponds to the graphene mask, and the pink zone denotes the first 4 layers of the MgO surface, all of which were subjected to a weak thermostat with a temperature damping parameter of 10<sup>7</sup> fs. In contrast, the bulk MgO in the purple zone was subjected to a stronger thermostat with a temperature damping parameter of 100 fs. This distinction mimics practical considerations in MBE systems, where the lower part of the substrate is heated directly by the heater to reach the target temperature. Consequently, stricter temperature control is required in the lower part of the substrate to match the experimental conditions, while a weak thermostat setting in other regions allows the rest of the system to be heated through the substrate, similar to MBE experimental setups.

In this simulated system, 10 Sn and 40 Se atoms were randomly positioned in vacuum above the masked substrate and the system temperature was set to 500 K, resulting in a layered SnSe structure after 250 ps, as illustrated in Figure 7b. Toward the end of the simulation, small clusters formed near the graphene layer. These clusters were mainly physisorbed to the pristine regions of the graphene mask by weak van der Waals interactions and then bounced off. Later, Se dimers and two small clusters were observed in vacuum.

In Figure 7c, we monitored the temperature profiles of each zone, including all four regions. The temperature of the kinetically energetic gas-phase precursors exhibited significant fluctuations, varying between 500 and 4500 K. Although the graphene layer was subjected to a weak thermostat, its proximity to the substrate allows heat transfer with the substrate, leading to cluster formation near its surface. Additionally, the temperature fluctuations are typically lower in the condensed phase (graphene layer and MgO substrate)

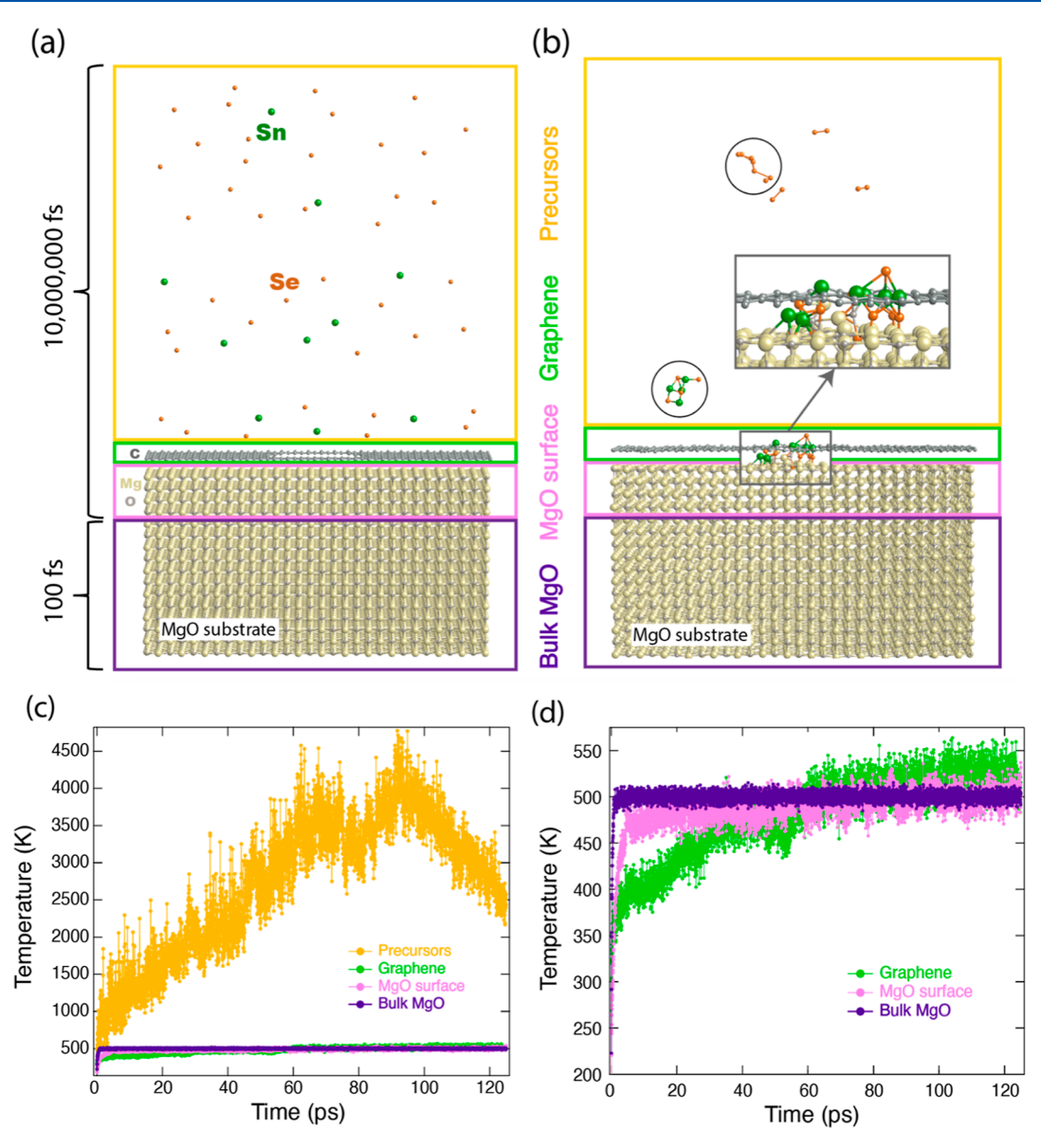


**Figure 7.** Simulation box was divided into 4 zones to illustrate the use of multiple thermostats in the simulation. The precursors (yellow zone), the graphene mask (green zone), and the first 4 layers of the bulk MgO substrate (pink zone) were all subjected to a temperature damping parameter of  $10^7$  fs. Only the bottom bulk MgO (purple zone) was set to 100 fs. (a) 10 Sn atoms and 40 Se atoms were randomly placed to observe their nucleation on MgO through the mask. (b) The layer-by-layer nucleation of SnSe after 250 ps simulation. (c) Temperature profiles of all regions as a function of time. (d) Temperature profiles of graphene, MgO surface, and bulk MgO. The precursors are not included in this plot for clarity.

than in the gas phase (precursors). In the condensed phase, the particles are more densely packed and have higher thermal transfer than the gas phase species. As a result, the graphene and the MgO surface, both subjected to a weak thermostat, exhibited relatively negligible temperature variations. This is because they are in condensed phases and close to the bulk MgO, which is under strong thermostat control. Their temperature profiles are highlighted in an additional plot in Figure 7d for clarity.

The use of multiple thermostats in a single simulation offers a transformative computational approach that is particularly critical for simulating the MBE nucleation and growth of thin films from the gas-phase precursors, where avoiding clustering in vacuum is a challenge. This challenge is particularly pronounced in MD simulations, where the time scales studied are typically in the nanosecond range. To capture meaningful events on this scale, a conventional approach is to increase the

density of the gas-phase precursors. However, such an increase in density inevitably leads to clustering, which deviates from an accurate representation of the MBE conditions. The introduction of weak thermostats for gas phase precursors, which effectively mitigate cluster formation and thus allow a more accurate representation of atomic spraying methods in MBE systems, promises to provide deeper insights into the intricacies of thin film nucleation dynamics in MD simulations.

# 4. CONCLUSION

By addressing the inherent challenges of SnSe epitaxial growth, such as island formation and nonuniformity, this study presents innovative solutions involving the use of masks for selective area nucleation. This method effectively confines nucleation to predetermined areas, resulting in more crystalline phases compared to nucleation on a bare substrate. The investigation also explores the effect of mask thickness,

revealing a preference for a single-layer graphene mask that facilitates the growth of crystalline SnSe structures.

Additionally, the influence of thermostat strength in Sn/Se gas phase simulations was investigated. The results suggest that the use of a weak thermostat for precursors prevents clustering. This approach was further applied to simulate SnSe nucleation systems, demonstrating the effectiveness of multiple thermostats to mimic experimental MBE setups.

In conclusion, this work contributes atomic-scale insights into the mechanisms governing SnSe nucleation. The proposed methods involving masks and thermostat control offer innovative strategies for achieving controlled nucleation and improved film quality in SnSe thin film synthesis, which hold promise for diverse applications.

# ASSOCIATED CONTENT

# **5** Supporting Information

The Supporting Information is available free of charge at https://pubs.acs.org/doi/10.1021/acs.jpcc.4c03096.

Figure S1: Initial configuration of SnSe nucleation on MgO with a graphene mask; Figure S2: Radial distribution function of the amorphous Sn<sub>x</sub>Se<sub>y</sub> structure; Figure S3: Snapshots from additional simulations showing consistent layering of Se and Sn; Figure S4: Alternative views of the final Sn<sub>x</sub>Se<sub>y</sub> structures; ReaxFF force field parameters for the Sn/Se/Mg/O/C system (PDF)

#### AUTHOR INFORMATION

# **Corresponding Author**

Adri C. T. van Duin – Department of Mechanical Engineering, The Pennsylvania State University, University Park, Pennsylvania 16802, United States; oorcid.org/ 0000-0002-3478-4945; Email: acv13@psu.edu

#### **Authors**

Benazir Fazlioglu-Yalcin – Department of Physics, Harvard University, Cambridge, Massachusetts 02138, United States

Mengyi Wang — Department of Materials Science and Engineering, The Pennsylvania State University, University Park, Pennsylvania 16802, United States; orcid.org/0000-0002-1548-5886

Nadire Nayir — Department of Physics Engineering, Istanbul Technical University, Istanbul 34469, Turkey; Department of Mechanical Engineering, The Pennsylvania State University, University Park, Pennsylvania 16802, United States;
ocid.org/0000-0002-3621-2481

Stephanie Law — Department of Materials Science and Engineering, The Pennsylvania State University, University Park, Pennsylvania 16802, United States; ⊚ orcid.org/0000-0002-5087-6663

Complete contact information is available at: https://pubs.acs.org/10.1021/acs.jpcc.4c03096

#### **Author Contributions**

<sup>1</sup>B.F-Y and M.W these authors contributed equally.

The authors declare no competing financial interest.

#### ACKNOWLEDGMENTS

This research was financially supported by the National Science Foundation (NSF) through the Pennsylvania State

University 2D Crystal Consortium-Materials Innovation Platform (2DCC-MIP) under NSF cooperative agreement numbers DMR-1539916 and DMR-2039351.

#### REFERENCES

- (1) Lewis, D. J.; Kevin, P.; Bakr, O.; Muryn, C. A.; Malik, M. A.; O'Brien, P. Routes to Tin Chalcogenide Materials as Thin Films or Nanoparticles: A Potentially Important Class of Semiconductor for Sustainable Solar Energy Conversion. *Inorg. Chem. Front.* **2014**, *1* (8), 577–598.
- (2) Dong, B.; Wang, Z.; Hung, N. T.; Oganov, A. R.; Yang, T.; Saito, R.; Zhang, Z. New Two-Dimensional Phase of Tin Chalcogenides: Candidates for High-Performance Thermoelectric Materials. *Phys. Rev. Mater.* **2019**, 3 (1), 013405.
- (3) Antunez, P. D.; Buckley, J. J.; Brutchey, R. L. Tin and Germanium Monochalcogenide IV–VI Semiconductor Nanocrystals for Use in Solar Cells. *Nanoscale* **2011**, *3* (6), 2399.
- (4) Banik, A.; Roychowdhury, S.; Biswas, K. The Journey of Tin Chalcogenides towards High-Performance Thermoelectrics and Topological Materials. *Chem. Commun.* **2018**, 54 (50), 6573–6590.
- (5) Shi, W.; Gao, M.; Wei, J.; Gao, J.; Fan, C.; Ashalley, E.; Li, H.; Wang, Z. Tin Selenide (SnSe): Growth, Properties, and Applications. *Adv. Sci.* **2018**, *5* (4), 1700602.
- (6) Xu, X.; Song, Q.; Wang, H.; Li, P.; Zhang, K.; Wang, Y.; Yuan, K.; Yang, Z.; Ye, Y.; Dai, L. In-Plane Anisotropies of Polarized Raman Response and Electrical Conductivity in Layered Tin Selenide. *ACS Appl. Mater. Interfaces* **2017**, *9* (14), 12601–12607.
- (7) Yang, S.; Liu, Y.; Wu, M.; Zhao, L.-D.; Lin, Z.; Cheng, H.; Wang, Y.; Jiang, C.; Wei, S.-H.; Huang, L.; et al. Highly-Anisotropic Optical and Electrical Properties in Layered SnSe. *Nano Res.* **2018**, *11* (1), 554–564.
- (8) Zhao, L.-D.; Tan, G.; Hao, S.; He, J.; Pei, Y.; Chi, H.; Wang, H.; Gong, S.; Xu, H.; Dravid, V. P.; et al. Ultrahigh Power Factor and Thermoelectric Performance in Hole-Doped Single-Crystal SnSe. *Science* **2016**, 351 (6269), 141–144.
- (9) Zhao, L.-D.; Lo, S.-H.; Zhang, Y.; Sun, H.; Tan, G.; Uher, C.; Wolverton, C.; Dravid, V. P.; Kanatzidis, M. G. Ultralow Thermal Conductivity and High Thermoelectric Figure of Merit in SnSe Crystals. *Nature* **2014**, *508* (7496), 373–377.
- (10) Minnam Reddy, V. R.; Lindwall, G.; Pejjai, B.; Gedi, S.; Kotte, T. R. R.; Sugiyama, M.; Liu, Z.-K.; Park, C. α-SnSe Thin Film Solar Cells Produced by Selenization of Magnetron Sputtered Tin Precursors. Sol. Energy Mater. Sol. Cells 2018, 176, 251–258.
- (11) Nandi, R.; Pawar, P. S.; Neerugatti, K. E.; Cho, J. Y.; Kim, S.; Cho, S. H.; Lee, Y. S.; Heo, J. Vapor-Transport-Deposited Orthorhombic-SnSe Thin Films: A Potential Cost-Effective Absorber Material for Solar-Cell Applications. *Sol. RRL* **2022**, *6* (2), 2100676.
- (12) Barrios-Salgado, E.; Nair, M. T. S.; Nair, P. K. Chemically Deposited SnSe Thin Films: Thermal Stability and Solar Cell Application. *ECS J. Solid State Sci. Technol.* **2014**, *3* (8), Q169–Q175.
- (13) Minnam Reddy, V. R.; Gedi, S.; Pejjai, B.; Park, C. Perspectives on SnSe-Based Thin Film Solar Cells: A Comprehensive Review. *J. Mater. Sci. Mater. Electron.* **2016**, 27 (6), 5491–5508.
- (14) Drozd, V. E.; Nikiforova, I. O.; Bogevolnov, V. B.; Yafyasov, A. M.; Filatova, E. O.; Papazoglou, D. ALD Synthesis of SnSe Layers and Nanostructures. *J. Phys. Appl. Phys.* **2009**, 42 (12), 125306.
- (15) Afrin, S.; Kuperman, N.; Solanki, R. Atomic Layer Deposition of 2-Dimensional, Semiconducting SnSe Thin Films. In 2018 IEEE 13th Nanotechnology Materials and Devices Conference (NMDC); IEEE: Portland, OR, 2018, pp 1—4..
- (16) Indirajith, R.; Srinivasan, T. P.; Ramamurthi, K.; Gopalakrishnan, R. S. Synthesis, deposition and characterization of tin selenide thin films by thermal evaporation technique. *Curr. Appl. Phys.* **2010**, *10* (6), 1402–1406.
- (17) Singh, J. P.; Bedi, R. K. Tin Selenide Films Grown by Hot Wall Epitaxy. *J. Appl. Phys.* **1990**, *68* (6), 2776–2779.
- (18) Boscher, N. D.; Carmalt, C. J.; Palgrave, R. G.; Parkin, I. P. Atmospheric Pressure Chemical Vapour Deposition of SnSe and

- SnSe2 Thin Films on Glass. *Thin Solid Films* **2008**, *516* (15), 4750–4757.
- (19) Zhong, Y.; Zhang, L.; Linseis, V.; Qin, B.; Chen, W.; Zhao, L.-D.; Zhu, H. High-Quality Textured SnSe Thin Films for Self-Powered, Rapid-Response Photothermoelectric Application. *Nano Energy* **2020**, *72*, 104742.
- (20) Anwar, S.; Gowthamaraju, S.; Mishra, B. K.; Singh, S. K.; Shahid, A.. Spray Pyrolysis Deposited Tin Selenide Thin Films for Thermoelectric Applications. *Mater. Chem. Phys.* **2015**, *153*, 236–242.
- (21) Narro-Rios, J. S.; Ramachandran, M.; Martínez-Escobar, D.; Sánchez-Juárez, A. Ultrasonic Spray Pyrolysis Deposition of SnSe and SnSe <sub>2</sub> Using a Single Spray Solution. *J. Semicond.* **2013**, 34 (1), 013001
- (22) Kumar, N.; Sharma, V.; Padha, N.; Shah, N. M.; Desai, M. S.; Panchal, C. J.; Protsenko, I. Yu Influence of the Substrate Temperature on the Structural, Optical, and Electrical Properties of Tin Selenide Thin Films Deposited by Thermal Evaporation Method. *Cryst. Res. Technol.* **2010**, *45* (1), 53–58.
- (23) Singh, K.; Soni; Anwar, S.; Dubey, P.; Mishra, S. K. Influence of Temperatures on Structure, Thermoelectric, and Mechanical Properties of Nanocrystalline SnSe Thin Films Deposited by Thermal Evaporation. *Mater. Today Commun.* **2022**, 32, 103880.
- (24) Fadavieslam, M. R.; Bagheri-Mohagheghi, M. M. Spray Pyrolysis of Tin Selenide Thin-Film Semiconductors: The Effect of Selenium Concentration on the Properties of the Thin Films. *J. Semicond.* 2013, 34 (8), 082001.
- (25) Chin, J. R.; Frye, M. B.; Liu, D. S.-H.; Hilse, M.; Graham, I. C.; Shallenberger, J.; Wang, K.; Engel-Herbert, R.; Wang, M.; Shin, Y. K.; Nayir, N.; Van Duin, A. C. T.; Garten, L. M. Self-Limiting Stoichiometry in SnSe Thin Films. *Nanoscale* **2023**, *15* (23), 9973–9984
- (26) Mortelmans, W.; Hilse, M.; Song, Q.; Jo, S. S.; Ye, K.; Liu, D.; Samarth, N.; Jaramillo, R. Measuring and Then Eliminating Twin Domains in SnSe Thin Films Using Fast Optical Metrology and Molecular Beam Epitaxy. ACS Nano 2022, 16 (6), 9472–9478.
- (27) Frezza, F.; Sánchez-Grande, A.; Ondráček, M.; Vondráček, M.; Chen, Q.; Stetsovych, O.; Villalobos-Vilda, V.; Tosi, E.; Palomares, F. J.; López, M. F.; et al. Epitaxial Growth and Characterization of SnSe Phases on Au(111). *J. Phys.: Condens. Matter* **2023**, *35* (33), 335001.
- (28) Zhang, Y.; Wang, C.; Tian, Q.; Meng, Q.; Zong, J.; Zhang, Y. Epitaxial Growth of Monolayer SnSe<sub>2</sub> Films on Gd-Intercalated Quasi-Free-Standing Monolayer Graphene with Enhanced Interface Adsorption. *J. Phys. Chem. C* **2022**, *126* (12), 5751–5758.
- (29) Allegretti, F. E.; Nishinaga, T. Periodic Supply Epitaxy: A New Approach for the Selective Area Growth of GaAs by Molecular Beam Epitaxy. *J. Cryst. Growth* **1995**, *156* (1–2), 1–10.
- (30) Lim, Z. H.; Manzo, S.; Strohbeen, P. J.; Saraswat, V.; Arnold, M. S.; Kawasaki, J. K. Selective Area Epitaxy of GaAs Films Using Patterned Graphene on Ge. *Appl. Phys. Lett.* **2022**, *120* (5), 051603.
- (31) Kapolnek, D.; Keller, S.; Vetury, R.; Underwood, R. D.; Kozodoy, P.; Den Baars, S. P.; Mishra, U. K. Anisotropic Epitaxial Lateral Growth in GaN Selective Area Epitaxy. *Appl. Phys. Lett.* **1997**, 71 (9), 1204–1206.
- (32) Bacchin, G.; Nishinaga, T. Dependence of the Degree of Selectivity on the Al Content during the Selective Area Growth of AlGaAs on GaAs(001) by PSE/MBE. *J. Cryst. Growth* **1998**, *191* (4), 599–606.
- (33) Bacchin, G.; Tsunoda, K.; Nishinaga, T. Selective Area Growth by Periodic Supply Molecular Beam Epitaxy. *Surf. Rev. Lett.* **1998**, *05* (03n04), 731–738.
- (34) Dede, D.; Glas, F.; Piazza, V.; Morgan, N.; Friedl, M.; Güniat, L.; Nur Dayi, E.; Balgarkashi, A.; Dubrovskii, V. G.; Fontcuberta I Morral, A. Selective Area Epitaxy of GaAs: The Unintuitive Role of Feature Size and Pitch. *Nanotechnology* **2022**, *33* (48), 485604.
- (35) Guo, Y.; Aisijiang, M.; Zhang, K.; Jiang, W.; Chen, Y.; Zheng, W.; Song, Z.; Cao, J.; Liu, Z.; Peng, H. Selective-Area Van Der Waals Epitaxy of Topological Insulator Grid Nanostructures for Broadband Transparent Flexible Electrodes. *Adv. Mater.* **2013**, 25 (41), 5959–5964.

- (36) Wang, N.; Yuan, X.; Zhang, X.; Gao, Q.; Zhao, B.; Li, L.; Lockrey, M.; Tan, H. H.; Jagadish, C.; Caroff, P. Shape Engineering of InP Nanostructures by Selective Area Epitaxy. *ACS Nano* **2019**, *13* (6), 7261–7269.
- (37) Heiß, M.; Riedlberger, E.; Spirkoska, D.; Bichler, M.; Abstreiter, G.; Morral, A. F. I. Growth Mechanisms and Optical Properties of GaAs-Based Semiconductor Microstructures by Selective Area Epitaxy. *J. Cryst. Growth* **2008**, *310* (6), 1049–1056.
- (38) Yuan, X.; Pan, D.; Zhou, Y.; Zhang, X.; Peng, K.; Zhao, B.; Deng, M.; He, J.; Tan, H. H.; Jagadish, C. Selective Area Epitaxy of III–V Nanostructure Arrays and Networks: Growth, Applications, and Future Directions. *Appl. Phys. Rev.* **2021**, *8* (2), 021302.
- (39) Noborisaka, J.; Motohisa, J.; Fukui, T. Catalyst-Free Growth of GaAs Nanowires by Selective-Area Metalorganic Vapor-Phase Epitaxy. *Appl. Phys. Lett.* **2005**, *86* (21), 213102.
- (40) Gao, Q.; Saxena, D.; Wang, F.; Fu, L.; Mokkapati, S.; Guo, Y.; Li, L.; Wong-Leung, J.; Caroff, P.; Tan, H. H.; et al. Selective-Area Epitaxy of Pure Wurtzite InP Nanowires: High Quantum Efficiency and Room-Temperature Lasing. *Nano Lett.* **2014**, *14* (9), 5206–5211.
- (41) Seidl, J.; Gluschke, J. G.; Yuan, X.; Naureen, S.; Shahid, N.; Tan, H. H.; Jagadish, C.; Micolich, A. P.; Caroff, P. Regaining a Spatial Dimension: Mechanically Transferrable Two-Dimensional InAs Nanofins Grown by Selective Area Epitaxy. *Nano Lett.* **2019**, *19* (7), 4666–4677.
- (42) Van Duin, A. C. T.; Dasgupta, S.; Lorant, F.; Goddard, W. A. ReaxFF: A Reactive Force Field for Hydrocarbons. *J. Phys. Chem. A* **2001**, *105* (41), 9396–9409.
- (43) Senftle, T. P.; Hong, S.; Islam, M. M.; Kylasa, S. B.; Zheng, Y.; Shin, Y. K.; Junkermeier, C.; Engel-Herbert, R.; Janik, M. J.; Aktulga, H. M.; Verstraelen, T.; Grama, A.; van Duin, A. C. T. The ReaxFF Reactive Force-Field: Development, Applications and Future Directions. *Npj Comput. Mater.* **2016**, *2* (1), 15011.
- (44) Nayir, N.; Mao, Q.; Wang, T.; Kowalik, M.; Zhang, Y.; Wang, M.; Dwivedi, S.; Jeong, G.-U.; Shin, Y. K.; Van Duin, A. Modeling and Simulations for 2D Materials: A ReaxFF Perspective. 2D Mater. 2023, 10 (3), 032002.
- (45) Dasgupta, N.; Chen, C.; Van Duin, A. C. T. Development and Application of ReaxFF Methodology for Understanding the Chemical Dynamics of Metal Carbonates in Aqueous Solutions. *Phys. Chem. Chem. Phys.* **2022**, 24 (5), 3322–3337.
- (46) Monti, S.; Corozzi, A.; Fristrup, P.; Joshi, K. L.; Shin, Y. K.; Oelschlaeger, P.; Van Duin, A. C. T.; Barone, V. Exploring the Conformational and Reactive Dynamics of Biomolecules in Solution Using an Extended Version of the Glycine Reactive Force Field. *Phys. Chem. Chem. Phys.* **2013**, *15* (36), 15062.
- (47) Kresse, G.; Furthmüller, J. Efficiency of Ab-Initio Total Energy Calculations for Metals and Semiconductors Using a Plane-Wave Basis Set. *Comput. Mater. Sci.* **1996**, *6* (1), 15–50.
- (48) Kresse, G.; Furthmüller, J. Efficient Iterative Schemes for *Ab Initio* Total-Energy Calculations Using a Plane-Wave Basis Set. *Phys. Rev. B* **1996**, *54* (16), 11169–11186.
- (49) Kresse, G.; Hafner, J. Ab Initio Molecular Dynamics for Liquid Metals. Phys. Rev. B 1993, 47 (1), 558-561.
- (50) Kresse, G.; Joubert, D. From Ultrasoft Pseudopotentials to the Projector Augmented-Wave Method. *Phys. Rev. B* **1999**, *59* (3), 1758–1775.
- (51) Kresse, G.; Hafner, J. Norm-Conserving and Ultrasoft Pseudopotentials for First-Row and Transition Elements. *J. Phys.: Condens. Matter* **1994**, 6 (40), 8245–8257.
- (52) Perdew, J. P.; Burke, K.; Ernzerhof, M. Generalized Gradient Approximation Made Simple. *Phys. Rev. Lett.* **1996**, 77 (18), 3865–3868.
- (53) Grimme, S.; Antony, J.; Ehrlich, S.; Krieg, H. A Consistent and Accurate *Ab Initio* Parametrization of Density Functional Dispersion Correction (DFT-D) for the 94 Elements H-Pu. *J. Chem. Phys.* **2010**, 132 (15), 154104.
- (54) ReaxFF 2023.1, SCM, Theoretical Chemistry; Vrije Universiteit: Amsterdam, The Netherlands. http://www.scm.com.

- (55) Li, F.; Wang, H.; Huang, R.; Chen, W.; Zhang, H. Recent Advances in SnSe Nanostructures beyond Thermoelectricity. *Adv. Funct. Mater.* **2022**, 32 (26), 2200516.
- (56) Kim, K. S.; Lee, D.; Chang, C. S.; Seo, S.; Hu, Y.; Cha, S.; Kim, H.; Shin, J.; Lee, J.-H.; Lee, S.; et al. Non-Epitaxial Single-Crystal 2D Material Growth by Geometric Confinement. *Nature* **2023**, *614* (7946), 88–94.
- (57) Leung, B.; Tsai, M.-C.; Song, J.; Zhang, Y.; Xiong, K.; Yuan, G.; Coltrin, M. E.; Han, J. Analysis of Channel Confined Selective Area Growth in Evolutionary Growth of GaN on SiO2. *J. Cryst. Growth* **2015**, 426, 95–102.
- (58) Adelung, R.; Aktas, O. C.; Franc, J.; Biswas, A.; Kunz, R.; Elbahri, M.; Kanzow, J.; Schürmann, U.; Faupel, F. Strain-Controlled Growth of Nanowires within Thin-Film Cracks. *Nat. Mater.* **2004**, *3* (6), 375–379.
- (59) Hersee, S. D.; Sun, X.; Wang, X. The Controlled Growth of GaN Nanowires. *Nano Lett.* **2006**, *6* (8), 1808–1811.
- (60) Soo, M. T.; Zheng, K.; Gao, Q.; Tan, H. H.; Jagadish, C.; Zou, J. Growth of Catalyst-Free Epitaxial InAs Nanowires on Si Wafers Using Metallic Masks. *Nano Lett.* **2016**, *16* (7), 4189–4193.
- (61) Bai, J.; Duan, X.; Huang, Y. Rational Fabrication of Graphene Nanoribbons Using a Nanowire Etch Mask. *Nano Lett.* **2009**, 9 (5), 2083–2087.
- (62) Choi, D. S.; Balandin, A. A.; Leung, M. S.; Stupian, G. W.; Presser, N.; Chung, S. W.; Heath, J. R.; Khitun, A.; Wang, K. L. Transport Study of a Single Bismuth Nanowire Fabricated by the Silver and Silicon Nanowire Shadow Masks. *Appl. Phys. Lett.* **2006**, 89 (14), 141503.
- (63) Cheng, H.; DePuydt, J. M.; Haase, M. A.; Potts, J. E. Molecular-Beam Epitaxy Growth of ZnSe Using a Cracked Selenium Source. *J. Vac. Sci. Technol. B Microelectron. Process. Phenom.* **1990**, 8 (2), 181–186.
- (64) Liu, D. S. H.; Hilse, M.; Engel-Herbert, R. Sticking Coefficients of Selenium and Tellurium. *J. Vac. Sci. Technol. Vac. Surf. Films* **2021**, 39 (2), 023413.